Comparative study of structural and magnetic properties of Ni and La substituted calcium hexaferrite

V. S. Shinde[1], S. G. Dahotre[2]*

[1]K.E.S. Anandibai Pradhan Science College, Department of Physics, Nagothane (M.S.), India

[2]Dr. Babasaheb Ambedkar Technological University, Department of Physics, Lonere (M.S.), India

Abstract

Ni and La substituted M-type Ca hexaferrite of composition $CaNi_1Fe_{11}O_{19}$ and $CaLa_1Fe_{11}O_{19}$ were synthesized by sol-gel auto combustion method using metal nitrates as oxidants and citric acid as reducing agent. The prepared samples were characterized by X-ray diffraction (XRD), scanning electron microscopy (SEM), Fourier transform infrared spectroscopy (FTIR), energy dispersive X-ray analysis (EDAX), and vibrating sample magnetometry (VSM). XRD study revealed that both samples had lattice parameters a and c within the range of M-type hexaferrite. The SEM micrographs displayed grains having irregular shapes and sizes in the nanometer range. FTIR peaks confirmed the structure of M-type hexaferrite. EDAX spectra showed the homogeneous distribution of ions in both samples. In $CaNi_1Fe_{11}O_{19}$, we found saturation magnetization (M_s) of 12.18 emu/g and coercivity (H_c) of 193.2 Oe. On the other hand, in $CaLa_1Fe_{11}O_{19}$, we found M_s of 0.55 emu/g and H_c of 404.4 Oe. Saturation magnetization and coercivity values obtained for La substituted M-type Ca hexaferrite are suitable for low-density magnetic recording devices.

Keywords: M-type calcium hexaferrite, sol-gel, saturation magnetization, coercivity.

INTRODUCTION

Nowadays, the demand for microwave absorption devices and recording media is increasing tremendously due to the increase in high-frequency signals and to fulfill the requirement of strong growth of information. The materials with high saturation magnetization and low magnetic coercivity values are suitable to absorb high energy waves. Such materials can be used for high-frequency circuits and microwave devices [1, 2]. The material having coercivity values between 300 to 400 Oe can be used for low-density magnetic recording applications, while a coercivity value greater than 1000 Oe is required for high-density video recording applications [3]. The ferrite materials having low coercivity are beneficial for magnetic recording applications such as in hard disks, floppy disks, videotapes, etc. [4]. For data storage and re-recordable memory devices, saturation magnetization, as well as coercivity values, need to be low so that a small magnetic field is required to overwrite the data [5]. Low-cost, easy manufacturing, better structural, electrical, and magnetic properties are the most important parameters while considering material for a particular application. Hexagonal ferrites are one of the most important materials that fit these criteria [6]. M-type calcium hexaferrite $CaFe_{12}O_{19}$ exhibits high saturation magnetization, strong uniaxial crystalline anisotropy, and large coercivity. These ferrites are extensively used in permanent magnets, magnetic recording media, data storage devices, microwave components, high-frequency circuits, and operating devices [7].

Nandotaria et al. [8] studied the structural, magnetic, and dielectric properties of Mg substituted Sr-Cu hexaferrite synthesized via a one-step solvent-free synthesis technique. It has been found that the lattice parameters and lattice volume decrease with increasing Mg^{2+} ion substitution. This decrease is due to the smaller ionic radius of Mg^{2+} ions than Cu^{2+} ions, here, Mg^{2+} ions replace Cu^{2+} ions in the crystal structure. The c/a values were found to be lower than the standard value of 3.98 of M-type hexaferrite. The average crystallite size ranged between 31 to 54 nm. The morphology of the samples was almost the same and it exhibits hexagonal faceted structure. The maximum coercivity value was found to be 1995 Oe for the Mg^{2+} ion concentration x=0.3 [8]. Parmar et al. [9] studied the structural, magnetic, and dielectric properties of Cu substituted M-type Pb hexaferrite synthesized via a co-precipitation method. It has been found that, with increasing Cu^{2+} ion concentration from 0 to 1 in steps of 0.2, lattice parameters and lattice volume decrease. The position of (107) diffraction peak shifted towards higher angles with increasing Cu^{2+} ion concentration. These changes are due to the smaller ionic radius of Cu^{2+} ions as compared to Fe^{3+} ions. The average crystallite sizes were between 39 to 43 nm for all samples. FTIR spectra show two absorption bands between 400 and 600 cm^{-1}, which confirm the formation of M-type hexaferrite. The small value of the squareness ratio (M_r/M_s<0.5) indicates a multi-domain structure for all samples. The saturation magnetization was found to increase while the coercivity value decreased from 257 to 103 Oe with increasing Cu^{2+} ion concentration [9]. Rane et al. [10] synthesized single-phase polycrystalline M-type Ba hexaferrite via solution combustion synthesis using glycine as a fuel. It has been observed that the

**vikasshinde4126@gmail.com*

https://orcid.org/0000-0003-3822-8011

preparation conditions and variations in particle size change the magnetic properties. For the neutral precursor solution, higher saturation magnetization and coercivity values were obtained. Kaur et al. [11] synthesized Co-Zr doped nano-crystalline Sr hexaferrite via precursor sol-gel method and reported the effect of precursors such as citric acid, tartaric acid, and sucrose on the structural, magnetic, dielectric, microwave, and electromagnetic properties. It has been observed that the smallest particle size was obtained when sucrose precursor was used in the sol-gel method. It has also been observed that Co^{2+} and Zr^{4+} ions prefer different sites in different series with the same composition. The magnetic parameters such as saturation magnetization, coercivity, and remanent magnetization values were also different for the series of different precursors [11]. The magnetic properties of M-type of Ca hexaferrite can be changed with the substitution of divalent and trivalent metal ions such as Ni^{2+}, Zn^{2+}, Mn^{2+}, Co^{2+}, Cu^{2+}, La^{3+}, Nd^{3+}, Al^{3+}, Ga^{3+}, Cr^{3+}, and Pr^{3+} [12, 13].

In the current research, M-type calcium hexaferrite of composition $CaNi_1Fe_{11}O_{19}$ and $CaLa_1Fe_{11}O_{19}$ were synthesized by the sol-gel auto-combustion method. This method has advantages such as high homogeneity, high purity, and particle size in the nanometer range. It also gives better structural, magnetic, and dielectric properties [14-16]. The structural properties of the synthesized samples were studied by X-ray diffraction (XRD), scanning electron microscopy (SEM), Fourier transform infrared (FTIR) spectroscopy, and energy dispersive X-ray analysis (EDAX) while the magnetic properties were studied by vibrating sample magnetometry (VSM). The objective was to synthesize Ni and La substituted Ca hexaferrite with magnetic properties suitable for magnetic recording devices.

MATERIALS AND METHODS

The samples of M-type Ni and La substituted Ca hexaferrite of composition $CaNi_1Fe_{11}O_{19}$ and $CaLa_1Fe_{11}O_{19}$ were synthesized by the sol-gel auto-combustion method. A.R. grade iron nitrate [$Fe(NO_3)_3.9H_2O$, Merck, ≥99.95%], calcium nitrate [$Ca(NO_3)_2.4H_2O$, Merck, ≥99.95%], nickel nitrate [$Ni(NO_3)_2.6H_2O$, Merck, ≥99.95%], lanthanum nitrate [$La(NO_3)_3.9H_2O$, Merck, ≥99.95%], and citric acid monohydrate (Merck, ≥99.95%) were used as raw materials without any further purification.

In the sol-gel auto-combustion method, an exothermic reaction between metal salts, which acts as the oxidizing agent, and an organic fuel, which acts as a reducing agent, takes place. As the nitrate salts are water-soluble at low temperatures, they are generally used. A stoichiometric amount of calcium nitrate, iron nitrate, nickel/lanthanum nitrate, and citric acid were dissolved in double-filtered distilled water. The ratio of citric acid to metal nitrate ions was taken as 1:1. For the preparation of the $CaNi_1Fe_{11}O_{19}$ sample, 21.84 g of $Fe(NO_3)_3.9H_2O$, 1.43 g of $Ni(NO_3)_2.6H_2O$, 1.16 g of $Ca(NO_3)_2.4H_2O$, and 13.43 g of citric acid were taken. Also for the preparation of the $CaLa_1Fe_{11}O_{19}$ sample, 20.25 g of $Fe(NO_3)_3.9H_2O$, 1.97 g of $La(NO_3)_3.9H_2O$, 1.07 g of $Ca(NO_3)_2.4H_2O$, and 12.44 g of citric acid were taken. Ammonia solution (25%) was added dropwise to the sol with continuous stirring until the pH reached 7. The neutralized solution was then heated at 80 °C on a hot plate till it was converted into a viscous brown gel. The gel was heated in an oven at 150 °C to form a loose powder by the auto-combustion process. The powder was converted into fine particles by using a pestle and mortar. The fine particles were calcined at 950 °C in an electric furnace for 8 h to obtain ferrite nanoparticles.

The structural characterizations of the samples were performed using a diffractometer (X'Pert Pro, Panalytical) with CuKα radiation of wavelength 1.54184 Å. The scanning angle range was 10°-100° with a step of 0.0215°. Fourier transform infrared (FTIR) spectra were recorded using a spectrometer (Spectrum FT-IR, Perkin-Elmer) with KBr pellets in the range of 4000 to 400 cm^{-1} with a resolution of 1 cm^{-1}. The morphology and particle size were determined using SEM micrographs which were recorded using a scanning electron microscope (Quanta 200 FEG, FEI). The micrographs were recorded at a magnification of 40000x in a high vacuum. The EDAX analysis system worked as an integrated feature of the SEM where X-ray radiations released by a sample during electron beam bombardment were recorded. Magnetic properties of the samples were measured using a vibrating sample magnetometer (VSM 7410, Lake Shore) in the applied field from -15 to +15 kOe at room temperature. The crystallite size (D) was determined using the Scherrer equation with a constant k of 0.9 [17]:

$$D = \frac{k.\lambda}{\beta.\cos\theta} \quad (A)$$

where β is the full width at half maximum (FWHM), θ is the Bragg's angle of maximum intensity peak, and λ is the wavelength of CuKα radiation. The lattice constants (a and c) and lattice volume of the unit cell (V_{cell}) were calculated by:

$$\frac{1}{d^2} = \frac{3}{4}\left(\frac{h^2 + h.k + k^2}{a^2}\right) + \frac{l^2}{c^2} \quad (B)$$

$$V_{cell} = \frac{\sqrt{3}}{2} a^2 c \quad (C)$$

The X-ray density was determined with the help of the following expression [18]:

$$\rho_m = 2MW/(N_A.V) \quad (D)$$

where MW is the molecular weight of the composition and factor 2 is for two molecules of the material contained in one unit cell, N_A is the Avogadro's number, and V is the volume of the unit cell.

RESULTS AND DISCUSSION

The phase and structural composition of samples

were determined using XRD analysis. The X-ray diffractograms of Ni and La-doped M-type calcium hexaferrite are shown in Fig. 1. The observed peaks were matched with standard JCPDS file 84-0757 [19]. The highest intensity diffraction peak for the $CaNi_1Fe_{11}O_{19}$ sample was observed at the (202) plane, while for the $CaLa_1Fe_{11}O_{19}$ sample it was found at the (107) plane. The XRD patterns consisted of standard reflecting planes (006), (110), (107), (008), (202), (116), (205), (206), (1011), (214), (300), (218), and (2011), which belong to M-type hexaferrite [20, 21]. The Ni and La concentration showed a noticeable effect on diffraction peak intensity for (107) and (202) planes. The values of 2θ, d-spacing, full width at half maximum (FWHM), crystallite size, lattice parameters (a and c), lattice volume, c/a ratio, and X-ray density for Ni and La substituted Ca hexaferrite are given in Table I. It can be observed from X-ray diffraction patterns that the major (202) peak position was shifted to a higher angle with Ni^{2+} ion substitution. The shift in the peak position was due to the differences in ionic radii of Ni^{2+} and La^{3+} ions. This shift caused the uniform strain and elastic deformation in the lattice and gave rise to shrinkage in the lattice. As a result, interplanar spacing and lattice constant values in Ni substitution were smaller as compared to La substitution. A similar shift was reported in the literature [9, 22, 23].

It was observed that the lattice parameters (a and c) and lattice volume for La substituted calcium hexaferrite were higher than Ni substituted calcium hexaferrite, whereas the crystallite size was smaller in La substitution as compared to Ni substitution. In the present study, the lattice parameter a remained unchanged while lattice parameter c increased from 22.27 to 22.91 Å. In general hexagonal ferrite shows almost constant lattice parameter a and minor variation in c [24]. The Ni^{2+} (0.69 Å) ion replaced Fe^{3+} (0.64 Å) ion in $CaNi_1Fe_{11}O_{19}$. To compensate for the charge difference, some Fe^{3+} ions converted into Fe^{2+} (0.780 Å) ions [25]. On the other hand, the La^{3+} (1.16 Å) ion replaced the Ca^{2+} (1.12 Å) ion in $CaLa_1Fe_{11}O_{19}$. This was due to the nearly equal ionic radii of the La^{3+} ion and Ca^{2+} ion. To compensate for the charge, some Fe^{3+} ions were also converted into Fe^{2+} ions [26]. The increase in lattice parameters and lattice volume in La^{3+} ion substitution as compared to Ni^{2+} ion substitution was due to the differences in ionic radii of Ni^{2+} and La^{3+} ions [24, 25]. For M-type structure, the c/a ratio is approximately 3.98, but in our study, this ratio varied from 3.79 to 3.89, which implies that some distortion occurred in the crystal lattice after La and Ni substitution in prepared calcium hexaferrites [27, 28]. The X-ray density (ϱ_m) was observed to be smaller in Ni substitution as compared to La substitution. The decrease in the X-ray density was due to the higher rate of decrease of molecular weight as compared to the rate of decrease of cell volume when we substitute Ni in place of La [29].

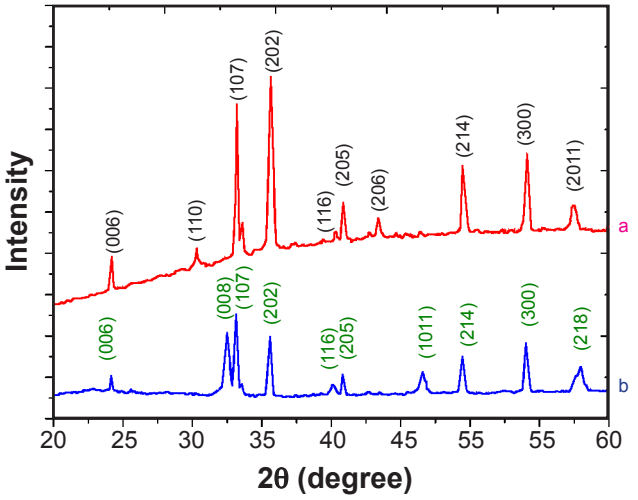

Figure 1: XRD patterns of: a) $CaNi_1Fe_{11}O_{19}$; and b) $CaLa_1Fe_{11}O_{19}$.

Scanning electron microscopy was used to examine the microstructure and surface of the prepared samples. Fig. 2 shows the SEM images and grain size distribution histograms of $CaNi_1Fe_{11}O_{19}$ and $CaLa_1Fe_{11}O_{19}$ samples. In the $CaNi_1Fe_{11}O_{19}$ sample, particles had irregular spherical shapes. Few particles were fused to form elongated rod-shaped secondary particles. Most of the primary particles had particle size from 75 to 150 nm and secondary particle size varied from 150 to 450 nm. The average particle size for $CaNi_1Fe_{11}O_{19}$ was 140 nm, while in the $CaLa_1Fe_{11}O_{19}$ sample, particles had a comparatively bigger size. They had irregular shapes and sizes. The average particle size in $CaLa_1Fe_{11}O_{19}$ was 274 nm. Sintering temperature would have increased the agglomeration of primary particles and it may have increased the particle size. The proper control of synthesis parameters in the sol-gel auto-combustion method gives the particle size in the nanometer range. The porous nature observed was due to the evolution of gases such as CO_2, N_2, etc., during the calcination [30].

FTIR spectra of Ni and La substituted calcium hexaferrite is shown in Fig. 3. The IR spectrum of both the samples showed two principal absorption bands between

Table I - Structural parameters of Ni and La substituted Ca hexaferrites.

Sample	2θ (degree)	d-spacing (Å)	FWHM, β (degree)	Crystallite size, D (nm)	Lattice parameter		c/a	Lattice volume (Å^3)	Density, ϱ_m (g/cm^3)
					a (Å)	c (Å)			
$CaNi_1Fe_{11}O_{19}$	33.18	2.698	0.129	59.3	5.87	22.27	3.79	664.7	5.081
$CaLa_1Fe_{11}O_{19}$	32.51	2.754	0.212	36.0	5.88	22.91	3.89	685.9	5.312

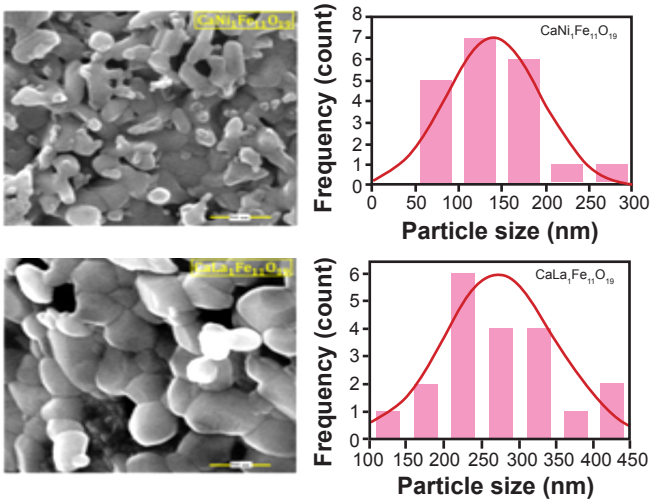

Figure 2: FE-SEM micrographs and grain size distribution histograms of $CaNi_1Fe_{11}O_{19}$ and $CaLa_1Fe_{11}O_{19}$ samples heated at 950 °C for 8 h (scale bar=500 nm).

429 and 520 cm^{-1}. These two vibration bands corresponded to intrinsic lattice vibrations of octahedral and tetrahedral clusters in hexaferrite. The absorption band between 600 and 400 cm^{-1} confirmed the formation of hexaferrite [5, 31]. The positions of two principal absorption bands for samples $CaNi_1Fe_{11}O_{19}$ and $CaLa_1Fe_{11}O_{19}$ are given in Table II. It was observed that with Ni and La substitution the positions of principal absorption bands changed. For Ni substitution, the position was shifted towards a higher wavenumber. This was because the wavenumber is inversely proportional to the atomic weight, which is higher for La than Ni [5, 32]. The absorption band around 2350 cm^{-1} was the O-C-O stretching vibration of a carbon dioxide molecule. The absorption band around 1760 cm^{-1} was the C=O stretching vibration of citric acid. The absorption band in the range of 1290-1550 cm^{-1} was the N-O stretching vibration of the nitro compound [33]. The observed results suggested that NO_3^- and CO_2^- groups participated in the self-combustion reaction [30].

To verify the existence of elements in the sample, the EDAX profiles of samples were recorded [34]. EDAX spectra for $CaNi_1Fe_{11}O_{19}$ and $CaLa_1Fe_{11}O_{19}$ powders are

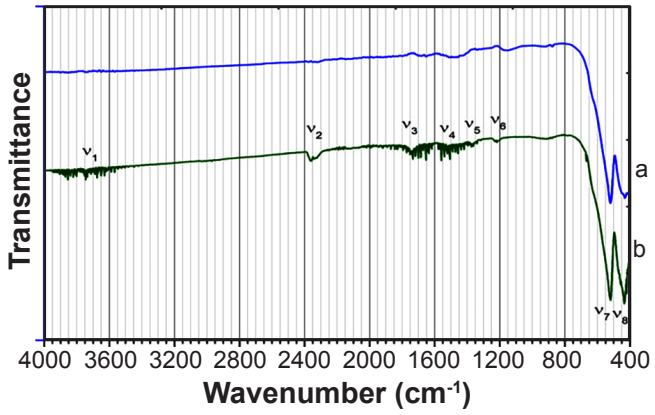

Figure 3: FTIR spectra of Ni and La substituted calcium hexaferrite: a) $CaNi_1Fe_{11}O_{19}$; and b) $CaLa_1Fe_{11}O_{19}$.

Table II - Two principal FTIR absorption bands for $CaNi_1Fe_{11}O_{19}$ and $CaLa_1Fe_{11}O_{19}$.

Sample	ν_7 (cm^{-1})	ν_8 (cm^{-1})
$CaNi_1Fe_{11}O_{19}$	521	461
$CaLa_1Fe_{11}O_{19}$	515	429

shown in Fig. 4. The theoretical and observed contents of elements for $CaNi_1Fe_{11}O_{19}$ and $CaLa_1Fe_{11}O_{19}$ hexaferrites are given in Table III. From the EDAX study, it was seen that the theoretical and measured contents of elements almost matched with each other. The small variations in the values were due to the applied acceleration voltage and the composition of elements used in the sample, which can change the content of the elements observed in an EDAX spectrum [35]. The EDAX spectra confirmed the almost homogeneous mixing of Ca, Ni, O, and Fe atoms in Ni substituted sample and homogeneous mixing of Ca, La, O, and Fe atoms in La substituted sample. It also confirmed the purity of the chemical compositions [36]. In the EDAX spectra, only the parent elements were found and hence no impurity elements were observed.

Typical room-temperature hysteresis loops for samples $CaNi_1Fe_{11}O_{19}$ and $CaLa_1Fe_{11}O_{19}$ prepared using the sol-gel auto-combustion method are shown in Fig. 5 and relevant magnetic data are presented in Table IV. Magnetic parameters obtained from the hysteresis loop showed that, for Ni^{2+} ion substitution, saturation magnetization (M_s) was higher than La^{3+} ion substitution, while the value of coercivity (H_c) was lower than La^{3+} ion substitution. There was no saturation in

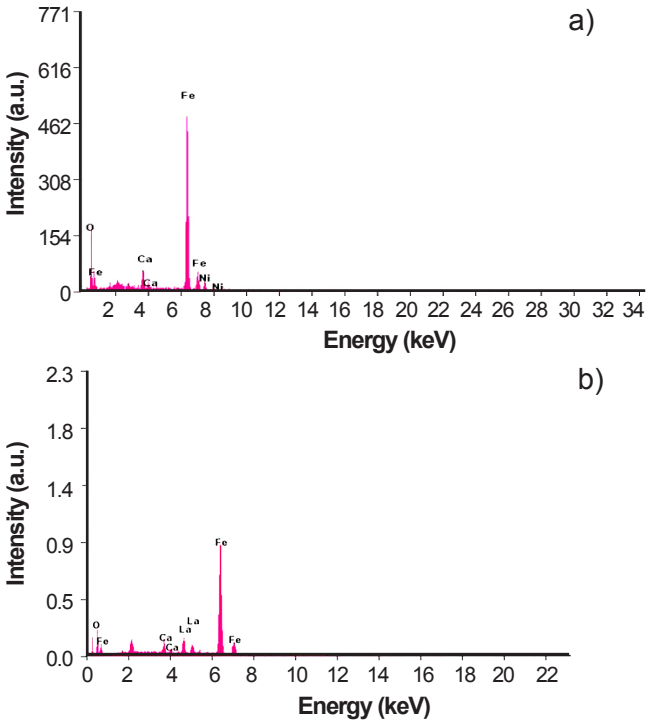

Figure 4: EDAX spectra of calcium hexaferrites: a) $CaNi_1Fe_{11}O_{19}$; and b) $CaLa_1Fe_{11}O_{19}$.

Table III - Theoretical and measured content of elements of $CaNi_1Fe_{11}O_{19}$ and $CaLa_1Fe_{11}O_{19}$ hexaferrites.

Sample	Theoretical (wt%)					Measured (wt%)				
	Fe	Ca	O	Ni	La	Fe	Ca	O	Ni	La
$CaNi_1Fe_{11}O_{19}$	60.40	3.94	29.88	5.77	-	67.94	5.02	20.36	6.68	-
$CaLa_1Fe_{11}O_{19}$	55.98	3.65	27.70	-	12.66	63.49	3.01	18.04	-	15.06

$CaLaFe_{11}O_{19}$ up to 15 kOe of the external magnetic field. Hence the maximum value of magnetization at 15 kOe external magnetic field was taken. In the case of a pure sample of $CaFe_{12}O_{19}$ without substitution, the values of M_s, H_c, M_r, and n_B were found to be 47.48 emu/g, 72.58 Oe, 3.16 emu/g, and 8.62 μ_B, respectively [27]. It was seen that with Ni^{2+} and La^{3+} ion substitution in Ca hexaferrite magnetic parameters M_s, M_r, and n_B decreased, while the value of coercivity increased.

In M-type hexaferrite, the c-axis is the easy axis of magnetization, and spins of the Fe^{3+} ions along with this axis have either parallel or antiparallel direction, which gives a net magnetic moment and are coupled by superexchange interactions through O^{2-} ions [37]. The distribution of Fe^{3+} ions along with different sites, having different geometry and spin orientation are given in Table V. There are five sites in which 12 Fe^{3+} ions are distributed. Among these five sites, the sites 12k, 2a, and $4f_2$ are octahedral sites, $4f_1$ is a tetrahedral site while 2b site is a trigonal bipyramidal site [38, 39]. Fe^{3+} ions distributed on 12k, 2a, and 2b sites have upward spin orientation along the c-axis, while those distributed on $4f_1$ and $4f_2$ sites have downward spin orientation along the c-direction [40]. The Gorter model suggests that a ferrimagnetic hexagonal structure is comprised of four parallel ($4f_1$ and $4f_2$) and eight antiparallel (12k, 2a, and 2b) spins [41]. Therefore, there is a total of 8 Fe^{3+} ions having a spin in an upward direction and 4 Fe^{3+} ions having a spin in a downward direction. The resultant of this orientation gives 4 Fe^{3+} ions spinning in an upward direction. Hence the net magnetic moment is 4x5 μ_B=20 μ_B in an upward direction (5 μ_B is the magnetic moment of Fe^{3+} ion).

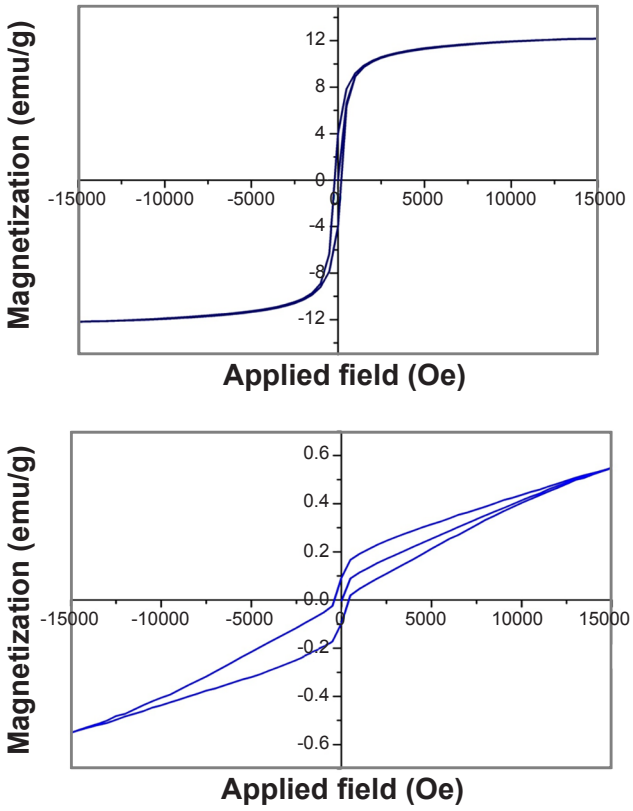

Figure 5: Hysteresis loop of magnetic powder: a) $CaNi_1Fe_{11}O_{19}$; and b) $CaLa_1Fe_{11}O_{19}$.

In the $CaFe_{12}O_{19}$ hexaferrite structure, Fe^{3+} ions have a magnetic moment of 5 μ_B. The magnetic moment of Ni^{2+} ions (2 μ_B) is smaller than that of Fe^{3+} ions. Roohani et al. [25] reported that the substituted Ni^{2+} ion enters the octahedral $4f_2$ state, which consists of Fe^{3+} ions having spin down orientation. As a result, the magnetic moment in the downward direction decreases (5 μ_B is reduced to 2 μ_B). The combined result is that the magnetic moment in the upward

Table V - Distribution of Fe^{3+} ions in M-type hexaferrite.

Site	Geometry	Number of Fe^{3+} ions	Spin
12k	Octahedral	6	↑
2a	Octahedral	1	↑
$4f_1$	Tetrahedral	2	↓
$4f_2$	Octahedral	2	↓
2b	Trigonal bipyramidal	1	↑

Table IV - Magnetic parameters of Ni and La substituted calcium hexaferrites.

Sample	M_s (emu/g)	H_c (Oe)	M_r (emu/g)	n_B (μ_B)	M_r/M_s
$CaNi_1Fe_{11}O_{19}$	12.18	193.2	4.00	2.22	0.33
$CaLa_1Fe_{11}O_{19}$	0.55	404.4	0.09	0.11	0.17

direction increases, due to which the saturation magnetization increases with Ni substitution [25]. On the other hand, the La^{3+} ion replaces the Ca^{2+} ion (2a site) in the structure of calcium hexaferrite. To compensate for the charge, some Fe^{3+} ions get converted into Fe^{2+} ions. The magnetic moment of Fe^{3+} and Fe^{2+} are 5 and 4 μ_B, respectively [42, 43]. The 12k and 2a sites are linked through superexchange interaction (Fe^{3+}-O^2-Fe^{3+}). This exchange gives the parallel arrangement of spins in the upward direction and increases the saturation magnetization. Due to the substitution of the La^{3+} ion in place of Ca^{2+} ion, Fe^{3+} ions get converted into Fe^{2+} ions and the superexchange interaction of 12k and 2a site (Fe^{3+}-O^{2-}-Fe^{2+}) becomes weaker [13]. The combined effect is that the saturation magnetization decreases with La^{3+} ion concentration. The other reason for a decrease in saturation magnetization in La substituted Ca hexaferrite as compared to Ni substituted Ca hexaferrite is that a substituted Ni is ferromagnetic material while La is a non-magnetic material. Satpute et al. [44] and Dahotre and Singh [45] observed that with non-magnetic material substitution the saturation magnetization decreases. Nandotaria et al. [8] also reported a sharp decrease in saturation magnetization of Mg substituted M-type Sr-Cu hexaferrite nanoparticles, where Mg^{2+} ion replaces Cu^{2+} ion.

The coercivity (H_c) of Ni substituted calcium hexaferrite was lower than La substituted hexaferrite due to the decrease of magnetocrystalline anisotropy. Rashad et al. [43] reported that the value of coercivity decreases with increasing the crystallite size. From Table I, it is clear that the crystallite size was smaller in La substitution as compared to Ni substitution, hence the coercivity increased. The grains of La substituted Ca hexaferrite were finer and hexagonal in shape as compared to Ni substituted Ca hexaferrite, which contained grains with irregular shapes. This also increased the coercivity in La substituted Ca hexaferrite. If the value of H_c (kOe) $>M_r/2$, the prepared nanomaterials can be useful for high-frequency applications [27]. In La substituted Ca hexaferrite this inequality holds well. Hence we can say that La substituted Ca hexaferrite can be useful for high-frequency applications. The ratio of M_r and M_s measures a squareness ratio (SQR) of the hysteresis loop and determines the hardness of the magnetic material. If this ratio is equal to or greater than 0.5, then the ceramic material is more anisotropic, hard, and single-domain. If this ratio is lower than 0.5, it forms a multi-domain structure [9, 46-48]. It was revealed in our study that both the samples had SQR less than 0.5, which confirmed the formation of soft ferrites with multi-domain structures. The Bohr magneton is directly proportional to the saturation magnetization and is given by:

$$n_B = \frac{MW.Ms}{5585} \qquad (E)$$

where MW is the molecular weight of the sample. The large difference in saturation magnetization of these two samples makes a large difference in the Bohr magneton. For La substituted Ca hexaferrite coercivity value obtained was 404 Oe, which can be suitable for low-density magnetic recording applications [3], while in Ni substituted Ca hexaferrite high value of saturation magnetization and small value of coercivity can be suitable for data storage and re-recordable memory devices [5]. From Table IV it is seen that the remanent magnetization (M_r) was lower for La substitution while it was higher for Ni substitution. Musa et al. [49] reported that the substitution of paramagnetic Al^{3+} ion in place of Fe^{3+} ion decreases the remanent magnetization. Here La^{3+} ion is also paramagnetic, having zero remanent magnetization. La^{3+} ion substitution decreased the ferromagnetic property and increased the paramagnetic property. On the other hand, Ni^{2+} ion is a ferromagnetic ion having a magnetic moment of 2 μ_B. Due to this, with Ni^{2+} ion substitution, the ferromagnetic property increases and hence the remanent magnetization [49].

CONCLUSIONS

Ni and La substituted Ca hexaferrites were synthesized by the auto-combustion method. The XRD data confirmed the formation of single-phase magnetoplumbite M-type hexaferrite. The lattice parameters (a, c) and lattice volume were lower in Ni substitution as compared to La substitution. The FTIR data confirmed the formation of M-type hexaferrite. SEM micrographs showed the grain size in the nano range. EDAX spectra gave the homogeneous distribution of ions in the mixture. With the substitution of Ni^{2+} and La^{3+} ions in Ca hexaferrite, the magnetic properties such as saturation magnetization, coercivity, and remanent magnetization changed. With Ni substitution, the ferromagnetic property increased while with La substitution paramagnetic property increased. With the substitution of non-magnetic (paramagnetic) ions, the value of saturation magnetization decreased while the value of coercivity increased, whereas with the substitution of ferromagnetic ion opposite results were observed. The observed results suggested that La substituted calcium hexaferrite can be suitable for low-density magnetic recording applications and high-frequency applications, while Ni substituted calcium hexaferrite can be suitable for data storage and re-recordable memory devices.

ACKNOWLEDGEMENT

The authors wish to acknowledge SAIF IITM, Madras for providing characterization facilities.

REFERENCES

[1] R.W. Chantrell, K. O'Grady, J. Phys. D Appl. Phys. **25**, 1 (1992) 1.
[2] P. Xu, X. Han, M. Wang, J. Phys. Chem. C **111**, 16 (2007) 5866.
[3] Widyastuti, N. Sasria, A. Marsha Alviani, M. Dwi Febri, P. Vania Mitha, J. Phys. Conf. Ser. **877** (2017) 12015.
[4] H.M. Khan, M.U. Islam, Y. Xu, M. Naeem Ashiq, I. Ali, M. Asif Iqbal, M. Ishaque, Ceram. Int. **40**, 5 (2014) 6487.

[5] A. Baykal, I.A. Auwal, S. Güner, H. Sözeri, J. Magn. Magn. Mater. **430** (2017) 29.
[6] A.D. Deshpande, K.G. Rewatkar, V.M. Nanoti, Mater. Today Proc. **4**, 11 (2017) 12174.
[7] R.B. Jotania, R.B. Khomane, C.C. Chauhan, S.K. Menon, B.D. Kulkarni, J. Magn. Magn. Mater. **320**, 6 (2008) 1095.
[8] R.A. Nandotaria, R.B. Jotania, C.S. Sandhu, M. Hashim, S.S. Meena, P. Bhatt, S.E. Shirsath, Ceram. Int. **44**, 4 (2018) 4426.
[9] D.D. Parmar, P.N. Dhruv, S.S. Meena, S. Kavita, C.S. Sandhu, M. Ellouze, R.B. Jotania, J. Electron. Mater. **49**, 10 (2020) 6024.
[10] V.A. Rane, S.S. Meena, S.P. Gokhale, S.M. Yusuf, G.J. Phatak, S.K. Date, J. Electron. Mater. **42**, 4 (2013) 761.
[11] P. Kaur, A. Duong, S.K. Chawla, S.B. Narang, S.S. Meena, SN Appl. Sci. **1**, 10 (2019) 1239.
[12] M.A. Almessiere, Y. Slimani, M. Sertkol, M. Nawaz, A. Baykal, I. Ercan, Results Phys. **13** (2019) 102244.
[13] Y. Yang, J. Shao, F. Wang, D. Huang, J. Ceram. Process. Res. **18**, 7 (2017) 501.
[14] F. Nakagomi, P.E.N. de Souza, T.J. Castro, V.K. Garg, A.C. Oliveira, F.C.E. Silva, A. Franco, P.C. Morais, S.W. da Silva, J. Alloys Compd. **842** (2020) 155751.
[15] T.J. Castro, P.A.M. Rodrigues, A.C. Oliveira, F. Nakagomi, J. Mantilla, J.A.H. Coaquira, A. Franco Júnior, H.V.S. Pessoni, P.C. Morais, S.W. da Silva, J. Appl. Phys. **121**, 1 (2017) 13904.
[16] S.W. da Silva, F. Nakagomi, M.S. Silva, A. Franco, V.K. Garg, A.C. Oliveira, P.C. Morais, J. Nanopart. Res. **14**, 4 (2012) 798.
[17] P. Shepherd, K.K. Mallick, R.J. Green, J. Magn. Magn. Mater. **311**, 2 (2007) 683.
[18] M. Aziz, S. Atiq, S. Riaz, S. Naseem, IOP Conf. Ser. Mater. Sci. Eng. **60** (2014) 12045.
[19] V.P. Singh, G. Kumar, A. Kumar, R.S. Rai, M.A. Valente, K.M. Batoo, R.K. Kotnala, M. Singh, Ceram. Int. **42**, 4 (2016) 5011.
[20] F.N. Tenorio Gonzalez, A.M. Bolarín Miró, F. Sánchez De Jesús, C.A. Cortés Escobedo, S. Ammar, J. Magn. Magn. Mater. **407** (2016) 188.
[21] Ch. Mamatha, M. Krishnaiah, C.S. Prakash, Int. J. Adv. Sci. Techn. Res. **5**, 5 (2015) 42.
[22] N. Suo, A. Sun, L. Yu, Z. Zuo, X. Zhao, W. Zhang, Y. Zhang, L. Shao, Z. Dang, Appl. Phys. A **126**, 3 (2020) 183.
[23] S.K. Chawla, S.S. Meena, P. Kaur, R.K. Mudsainiyan, S.M. Yusuf, J. Magn. Magn. Mater. **378** (2015) 84.
[24] A.P. Bhat, S.J. Dhoble, D.K. Sahu, K.G. Rewatkar, Mater. Today Proc. **5**, 10 (2018) 22181.
[25] E. Roohani, H. Arabi, R. Sarhaddi, Int. J. Mod. Phys. B **32**, 1 (2018) 1750271.
[26] P. Kaur, S.B. Narang, S. Bahel, J. Supercond. Nov. Magn. **30**, 8 (2017) 2239.
[27] C.C. Chauhan, A.R. Kagdi, R.B. Jotania, A. Upadhyay, C.S. Sandhu, S.E. Shirsath, S.S. Meena, Ceram. Int. **44**, 15 (2018) 17812.
[28] C.D. Patel, P.N. Dhruv, S.S. Meena, C. Singh, S. Kavita, M. Ellouze, R.B. Jotania, Ceram. Int. **46**, 16 (2020) 24816.
[29] A.R. Bhalekar, L.N. Singh, J. Supercond. Nov. Magn. **33**, 6 (2020) 1859.
[30] E. Khorashadizade, H. Arabi, A. Yousefi, Appl. Mech. Mater. **229** (2012) 210.
[31] S. Dafe, M. Salunkhe, Int. J. Eng. Res. Technol. **4**, 11 (2015) 345.
[32] R.K. Mudsainiyan, S.K. Chawla, S.S. Meena, N. Sharma, R. Singh, A. Das, Ceram. Int. **40**, 10 (2014) 16617.
[33] LibreTexts, "Chemistry", https://chem.libretexts.org.
[34] B. Chandra Babu, K. Naveen Kumar, B.H. Rudramadevi, S. Buddhudu, Ferroelectr. Lett. Sect. **41**, 1-3 (2014) 28.
[35] N.M. Deraz, A. Alarifi, J. Anal. Appl. Pyrolysis **94** (2012) 41.
[36] N. Rezlescu, F. Rezlescu, P.D. Poda, C. Doroftei, M. Ignat, Rom. Rep. Phys. **65**, 4 (2013) 1348.
[37] Q. Li, J. Song, M. Saura-Múzquiz, F. Besenbacher, M. Christensen, M. Dong, Sci. Rep. **6**, 1 (2016) 25985.
[38] D.H. Choi, S.Y. An, S.W. Lee, I.B. Shim, C.S. Kim, Phys. Status Solidi B **241**, 7 (2004) 1736.
[39] P. Kaur, S.K. Chawla, S.S. Meena, S.M. Yusuf, K. Pubby, S.B. Narang, Ceram. Int. **43**, 1 (2017) 590.
[40] D. Chen, Y. Liu, Y. Li, K. Yang, H. Zhang, J. Magn. Magn. Mater. **337-338** (2013) 65.
[41] P. Kaur, S.K. Chawla, S.S. Meena, S.M. Yusuf, S.B. Narang, Ceram. Int. **42**, 13 (2016) 14475.
[42] F. Guo, X. Wu, G. Ji, J. Xu, L. Zou, S. Gan, J. Supercond. Nov. Magn. **27**, 2 (2013) 411.
[43] M.M. Rashad, H.M. El-Sayed, M. Rasly, A.A. Sattar, I.A. Ibrahim, J. Mater. Sci. Mater. Electron. **24**, 1 (2012) 282.
[44] S.S. Satpute, S.R. Wadgane, S.R. Kadam, D.R. Mane, R.H. Kadam, Cerâmica **65**, 374 (2019) 274.
[45] S.G. Dahotre, L.N. Singh, Arch. Phys. Res. **2**, 1 (2011) 81.
[46] A.R. Kagdi, N.P. Solanki, F.E. Carvalho, S.S. Meena, P. Bhatt, R.C. Pullar, R.B. Jotania, J. Alloys Compd. **741** (2018) 377.
[47] D.D. Parmar, P.N. Dhruv, S.S. Meena, S. Kavita, C.S. Sandhu, M. Ellouze, R.B. Jotania, J. Electron. Mater. **49**, 10 (2020) 6024.
[48] R.K. Mudsainiyan, S.K. Chawla, S.S. Meena, J. Alloys Compd. **615** (2014) 875.
[49] M.A. Musa, R.S. Azis, N.H. Osman, J. Hassan, M.M. Dihom, J. Aust. Ceram. Soc. **54**, 1 (2018) 55.
(Rec. 27/10/2020, Rev. 08/02/2021, 18/02/2021, Ac. 22/02/2021)